Magnetic Resonance in Medicine 58:582–591 (2007)

Parallel Image Reconstruction Using B-Spline Approximation (PROBER)

Jan Petr,[1*] Jan Kybic,[1] Michael Bock,[2] Sven Müller,[2] and Václav Hlaváč[1]

A new reconstruction method for parallel MRI called PROBER is proposed. The method PROBER works in an image domain similar to methods based on Sensitivity Encoding (SENSE). However, unlike SENSE, which first estimates the spatial sensitivity maps, PROBER approximates the reconstruction coefficients directly by B-splines. Also, B-spline coefficients are estimated at once in order to minimize the reconstruction error instead of estimating the reconstruction in each pixel independently (as in SENSE). This makes the method robust to noise in reference images. No presmoothing of reference images is necessary. The number of estimated parameters is reduced, which speeds up the estimation process. PROBER was tested on simulated, phantom, and in vivo data. The results are compared with commercial implementations of the algorithms SENSE and GRAPPA (Generalized Autocalibrating Partially Parallel Acquisitions) in terms of elapsed time and reconstruction quality. The experiments showed that PROBER is faster than GRAPPA and SENSE for images wider than 150 × 150 pixels for comparable reconstruction quality. With more basis functions, PROBER outperforms both SENSE and GRAPPA in reconstruction quality at the cost of slightly increased computational time. Magn Reson Med 58:582–591, 2007. © 2007 Wiley-Liss, Inc.

Key words: parallel imaging; SENSE; B-splines; GRAPPA

Parallel MRI is a technique that exploits the intrinsic spatial encoding of multiple receiver coils with distinct spatial sensitivities to speed up MRI data acquisition (1–10). The increase in data acquisition speed is achieved by sampling the *k*-space more sparsely in the phase-encoding direction. Due to this subsampling, the images are affected by aliasing. The missing *k*-space information is synthesized using sensitivity information from the receiver coils (called array coils). Several different reconstruction algorithms have been proposed working either in the *k*-space (frequency domain) or in the spatial domain. High image quality and short reconstruction times are desirable. However, since the reconstruction problem can be ill-conditioned, these requirements are sometimes difficult to fulfill.

With the Simultaneous Acquisition of Spatial Harmonics (SMASH) algorithm (1) the missing phase-encoding steps are reconstructed directly in the *k*-space using a linear combination of the neighboring phase-encoding lines. The original SMASH method is restricted to coil configurations with sensitivity profiles that are close to harmonic functions. SMASH was later improved to allow reconstruction with arbitrary coil configurations (2,3). The autocalibration process was introduced in AUTO-SMASH and Variable Density AUTO-SMASH (4,5) where fully sampled portions of *k*-space are used to calibrate the method without having to extract and process sensitivity maps. A more precise blockwise reconstruction was proposed (6), and later as Generalized Autocalibrating Partially Parallel Acquisitions (GRAPPA) (7). In GRAPPA the unaliased images are reconstructed for each array-coil element separately and are subsequently combined using the conventional sum-of-squares (11).

The second group of reconstruction methods works in the spatial domain. Sensitivity Encoding (SENSE) (8) builds a generalized encoding matrix that transforms the homogeneous-sensitivity unaliased image to aliased array-coil images. The reconstruction matrix is obtained as the inverse of the generalized encoding matrix. For normal image sizes, the encoding matrix is too large to be inverted directly. In the case of Cartesian sampling, only a small number of pixels contribute to each aliased pixel and the encoding matrix is block-diagonal. Thus, the matrix inversion can be decomposed and the inversion can be performed independently for all small matrices corresponding to each pixel.

For non-Cartesian sampling, such as spiral or radial *k*-space trajectories, the encoding matrix cannot be decomposed since the value of each aliased pixel depends on a large number of pixels in the unaliased image. Furthermore, the dependency is not spatially invariant. Therefore, an iterative solution using conjugate-gradients method was proposed (9). However, the reconstruction time is too long to be used in clinical practice.

In this article a novel image-based reconstruction method based on our previous work (12,13), which takes advantage of the linearity and smoothness of the reconstruction transformation, is presented. A linear reconstruction transformation is estimated directly while minimizing a reconstruction-error criterion. This criterion penalizes the presence of aliasing artifacts and noise in the reconstructed images. Unlike the SENSE algorithm, the transformation is not estimated for each pixel independently. Instead, the reconstruction transformation is represented using suitable basis functions. The small number of reconstruction coefficients regularizes the reconstruction and makes the computations faster and more stable. We use B-splines as basis functions because of their known good approximation properties (15).

The new method, called *P*arallel MRI *Rec*onstruction Using *B*-splin*e* App*r*oximation (PROBER), is compared

[1]Czech Technical University in Prague, Faculty of Electrical Engineering, Department of Cybernetics, Center for Machine Perception, Praha, Czech Republic.

[2]German Cancer Research Center, Department of Medical Physics in Radiology, Heidelberg, Germany.

Grant sponsor: Czech Academy of Sciences; Grant number: 1ET101050403.

*Correspondence to: Jan Petr, Czech Technical University, Faculty of Electrical Engineering, Department of Cybernetics, Karlovo namesti 13, 121 35 Prague 2, Czech Republic. E-mail: petrj5@cmp.felk.cvut.cz

Received 15 February 2007; revised 8 June 2007; accepted 24 June 2007.

DOI 10.1002/mrm.21366

Published online in Wiley InterScience (www.interscience.wiley.com).

with commercial implementations of GRAPPA and SENSE using simulated, phantom, and in vivo images. The reconstruction speed of all methods is measured for various numbers of channels and image sizes.

THEORY

In parallel MRI, signals are acquired using several receiver coils. The complex image S_l obtained from the l-th receiver coil can be written as a pointwise product of the ideal image S and the sensitivity of the coil C_l:

$$S_l(x,y) = C_l(x,y)S(x,y). \quad [1]$$

To increase the acquisition speed, input images S_l are sampled in the k-space more sparsely, which results in a reduced field-of-view (FOV) in the phase-encoding direction (here the y direction) and in aliasing. Since the image information is recovered by a Fourier transform of the acquired signal, the relation between the aliased image S^A and the fully sampled image S is (10):

$$S^A(x,y) = \sum_{m=0}^{M-1} S\left(x, y + m\frac{Y}{M}\right), \quad [2]$$

where M is the acceleration factor (i.e., every M-th k-space line is retrieved), Y is the original FOV in the phase-encoding direction, and $y = 1, \ldots, \frac{Y}{M}$. The task of parallel MRI is to reconstruct an unaliased image $\hat{S}$ from a set of input images S_l^A (aliased array-coil images) approximating the true image S.

PROBER Method

The PROBER reconstruction method is divided into two consecutive steps. In the estimation step, reference images without aliasing S and S_l are acquired and are used to estimate a reconstruction transformation α_l. In the reconstruction step, the transformation α_l is used to reconstruct an unaliased image $\hat{S}$ of a possibly different object from a set of array-coil images with aliasing S_l^A provided that the images S_l^A, S, and S_l are acquired using the same coil configuration.

Equations [1,2] are both linear in S, so the composite transformation from the ideal image S to the array-coil image with aliasing S_l^A is also linear. We assume that this composite transformation is invertible, which is an implicit assumption of all reconstruction methods and is generally the case for any reasonable coil configuration. The inverse transformation can then be written as a linear transformation α_l that combines L input images S_l^A to form the reconstructed image $\hat{S}$:

$$\hat{S}\left(x, y + m\frac{Y}{M}\right) = \sum_{l=1}^{L} \alpha_l\left(x, y + m\frac{Y}{M}\right) S_l^A(x,y), \quad [3]$$

where $\alpha_l(x,y)$ are the complex weights for the l-th coil, $y = 1, \ldots, \frac{Y}{M}$ and $m = 1, \ldots, M$.

If the reference and input images S, S_l, and S_l^A display the same object, an estimate of α can be obtained by minimizing the difference between $\hat{S}$ and S. This minimization problem is analyzed below.

Perfect Reconstruction Conditions

Substitution of Eq. [2] in the reconstruction transformation equation (Eq. [3]) yields:

$$\begin{aligned} S\left(x, y + m\frac{Y}{M}\right) &\approx \hat{S}\left(x, y + m\frac{Y}{M}\right) \\ &= \sum_{l=1}^{L} \alpha_l\left(x, y + m\frac{Y}{M}\right) S_l^A(x,y) \\ &= \sum_{m'=0}^{M-1} \sum_{l=1}^{L} \alpha_l\left(x, y + m\frac{Y}{M}\right) S_l\left(x, y + m'\frac{Y}{M}\right). \end{aligned} \quad [4]$$

Intensity values at different spatial positions are in general independent. Namely, the values $S\left(x, y + m\frac{Y}{M}\right)$ and $S\left(x, y + m'\frac{Y}{M}\right)$ are independent for $m \neq m'$. Hence, for arbitrary S_l it must be valid that $\sum_l \alpha_l\left(x, y + m\frac{Y}{M}\right) S_l\left(x, y + m'\frac{Y}{M}\right) = 0$ for $m \neq m$, so that there is no aliasing. Combining this with Eq. [4] yields the perfect reconstruction conditions:

$$\sum_{l=1}^{L} \alpha_l\left(x, y + m\frac{Y}{M}\right) S_l\left(x, y + m'\frac{Y}{M}\right) = \delta_{m,m'} S\left(x, y + m\frac{Y}{M}\right), \quad [5]$$

where $\delta_{m,m'}$ is Kronecker's delta. Equation [5] states that the reconstruction $\hat{S}$ is equal to the reference S, yet there is no aliasing present.

Noise Propagation

An important image quality factor is the propagation of noise from the input images to the reconstructed image. It is assumed that the input images S_l^A contain i.i.d. zero-mean Gaussian noise in both the real and the imaginary parts. The real and the imaginary parts of the noise are uncorrelated and have the same variance σ_1^2. Then the noise in each pixel of the reconstructed image given by Eq. [3] is also Gaussian, with variance $\sigma_{\text{Rec}}^2(x,y)$:

$$\sigma_{\text{Rec}}^2(x,y) = \sum_{l=1}^{L} 2|\alpha_l(x,y)|^2 \sigma_l^2. \quad [6]$$

Equation [6] describes the propagation of noise from the input images to the reconstruction. This is similar to a geometry factor described by Pruessman et al. (8) that estimates the achievable signal-to-noise ratio (SNR) for a

given coil configuration. To obtain high-quality reconstruction the total noise variance $\sum_{x,y}\sigma^2_{\mathrm{Rec}}(x,y)$ should be minimized.

B-Spline Approximation

We assume that the coil sensitivities C_l (Eq. [1]) change slowly and smoothly in space and, consequently, the same holds for the reconstruction transformation α. Thus, the reconstruction transformation α (Eq. [3]) need not to be calculated at each point independently but it can be represented by smooth functions such as B-splines.

B-spline β^p of degree p is a piecewise polynomial function with compact support. B-splines are widely used for their good approximation properties (15). In this work, uniformly spaced shifted cubic B-splines β^3 have been chosen as basis functions. One-dimensional B-spline functions $\psi_i(y)$ and $\psi_j(x)$ are evenly spaced over the image in the phase and frequency-encoding directions, respectively.

$$\varphi_i(y) = \beta^3(y/H_y - i + 2)$$

$$H_y = Y/(1 - 3) \qquad [7]$$

where $i=1,\ldots,I$, I is the number of B-splines in the phase-encoding direction, and Y is the image size. The basis $\psi_j(x)$ is obtained similarly. Note that the parameters are chosen so that at least four B-splines contribute at each pixel position to ensure full representability (15). The reconstruction transformation α_l is represented as a linear combination of tensor products of the basis functions $\psi_i(x)$ and $\psi_j(y)$:

$$\alpha_l(x,y) = \sum_{i=1}^{I}\sum_{j=1}^{J} g_{ijl}\varphi_i(y)\varphi_j(x), \qquad [8]$$

where J is the number of B-splines used in the readout direction x and g_{ijl} are complex B-spline coefficients that represent α_l for the l-th coil. Typically, from 4 to 15 B-splines are used in each dimension.

Reconstruction Error

We define a squared reconstruction error e consisting of a deterministic and a stochastic part. The deterministic part penalizes the deviation from the perfect reconstruction conditions (Eq. [5]), whereas the stochastic part minimizes the total noise variance σ^2_{Rec} (Eq. [6]):

$$e = \sum_{m,m'=0}^{M-1}\left\| \sum_{l=1}^{L}\alpha_l\left(x,y + m\frac{Y}{M}\right)S_l\left(x,y + m'\frac{Y}{M}\right) - \delta_{m,m'}S\left(x,y + m\frac{Y}{M}\right)\right\|^2 + \sum_{m=0}^{M-1}\left\| \sum_{l=1}^{L}\left|\alpha_l\left(x,y + m\frac{Y}{M}\right)\right|^2\sigma_l^2\right\|^2 \qquad [9]$$

where $\|\ldots\|^2$ is an l_2 norm over all $x = 1,\ldots,X$ and $y = 1,\ldots,\frac{Y}{M}$.

The aim of the estimation process is to find parameters g_{ijl} that minimize the error e. For optimal g_{ijl} the derivative with respect to the complex conjugate g^*_{ijl} must be zero. This yields a system of linear equations (13):

$$\mathbf{Ag} = \mathbf{B}, \qquad [10]$$

where $\mathbf{g}$ is a vector of the unknowns g_{ijl} with length $I \times J \times L$. The matrix $\mathbf{A}$ is Hermitian and positive definite (13), so it can be solved using the Cholesky decomposition (16,17). The solution vector $\mathbf{g}$ defines the reconstruction transformation α_l (Eq. [3]) which is used to reconstruct the unaliased image from the set of input images (Eq. [3]).

Autocalibration

So far, the reconstruction coefficients g_{ijl} were estimated from full-resolution unaliased reference images S_l and S. However, as the sensitivity information is changing slowly in space, it is sufficient to use low-resolution images for the estimation step (18). The size of the B-spline basis must be adopted accordingly in the estimation phase by setting Y (the estimation grid size) in Eq. [7]. The reconstruction is then performed using the full-resolution images S_l^A (Eq. [3]), where the reconstruction transformation α is calculated using the full-resolution B-spline basis (Eq. [7]).

Similar to existing autocalibration techniques for GRAPPA and SMASH, low-resolution images without aliasing can be acquired at the same time as the parallel imaging data using variable-density k-space sampling (5,7,18). The k-space center is fully sampled while the rest of the k-space is undersampled with the acceleration factor M. The size of the center is usually relatively small and the total acquisition time is therefore not significantly increased.

Construction of the matrix $\mathbf{A}$ (Eq. [10]) involves a dot product of the B-spline basis $\psi_j(x)$ and $\psi_j(y)$ with the image function S_l. The size of the reference image S_l is usually very small (24×24 pixels in our experiments) and sampling the B-splines with a similar resolution is often not satisfactory. For higher accuracy and reconstruction quality, the B-splines and the low-resolution reference images S_l are resampled at a higher resolution—the estimation grid size is increased (14).

Reference Image Choice

In parallel MRI, the homogeneous-sensitivity reference image is usually not acquired. Instead, the reference image is approximated as the sum-of-squares (SoS) of the array-coil images $S(x,y) = \sqrt{\sum_l S_l^2(x,y)}$. SoS image is an optimal combination of array-coil images with respect to image SNR in the case of unknown sensitivities (11,18).

The second possibility is to consider each array-coil image S_l in turn to be the reference image (7). Its relation to all other array-coil images $S_{l'}$ (similarly as in Eq. [1]) is given by:

$$S_{l'}(x,y) = C_{l'}(x,y)S(x,y) = C_{l'}(x,y)C_l^{-1}(x,y)S_l(x,y)$$

$$= C_{ll'}(x,y)S_l(x,y), \qquad [11]$$

where $C_{lj'}$ are modified sensitivities. The value of sensitivity $C_{lj'}$ goes to infinity for pixels where C_l is zero. However, for a reasonable coil configuration there are coils with nonzero sensitivity C_l in each pixel, and thus the reconstruction is feasible by assigning the reconstruction transformation a small or zero value in these pixels. Furthermore, the values of $C_{lj'}$ are not computed explicitly. Instead, the reconstruction error is minimized using directly the images S_l and $S_{l'}$. The reconstruction transformation α is estimated and the unaliased images $\hat{S}_l$ are reconstructed separately for each array-coil image S_l. The final image $\hat{S}$ is computed as an SoS of the reconstructed array-coil images $\hat{S}$. B-spline approximation (Eq. [8]) and the stochastic criterion (Eq. [6]) regularize the reconstruction in points where the sensitivity C_l is close to zero for some l.

MATERIALS AND METHODS

The PROBER algorithm was compared with GRAPPA (7) and SENSE (8) using simulated images and phantom and in vivo MR data. Variable-density images with acceleration factors of 2 and 4 were used as inputs. The size of the fully sampled k-space center was 24 lines. The reconstruction quality was compared using SNR:

$$SNR = 20\log_{10}\sqrt{\|S^G\|^2_{x,y}/\|\hat{S} - S^G\|^2_{x,y}}, \qquad [12]$$

where $\hat{S}$ is the reconstructed image and S^G is the homogeneous-sensitivity full-FOV image. Background regions were identified by thresholding (below 2% of the mean image value) and excluded from the SNR calculation.

Simulated Images

The algorithms were tested on nine sets of simulated images where SNR could be evaluated accurately and the noise level could be controlled. Homogeneous-sensitivity images and sensitivity maps used to generate the simulated images were extracted from the phantom and in vivo images described in the following sections. Homogeneous-sensitivity image S^G was obtained as the SoS of the array-coil images. Intensity bias caused by the SoS combination was corrected using a nonparametric intensity correction method (19). The image intensities were scaled to a mean value of 0.5 for each image. Sensitivity maps were obtained by dividing the array-coil images by a homogeneous-sensitivity image S^G. The maps were filtered to remove noise (8).

Images of 256×256 pixels were generated and complex Gaussian noise was added. The reconstruction transformation was estimated using reference images with the noise variance set to $1 \cdot 10^{-3}$. Then the reconstruction transformation was used to reconstruct the input images with the noise variance varying from 0 to $8 \cdot 10^{-3}$. The presence of aliasing artifacts in the reconstruction was assessed by evaluating SNR (Eq. [12]) for noise-free input images. Noise amplification in the reconstruction was tested by monitoring the reconstruction SNR with an increasing level of noise in the input images.

Phantom Images

Phantom images were acquired on a clinical 1.5T MR system (Magnetom Symphony, Siemens Medical Solutions, Erlangen, Germany) using a spoiled gradient echo pulse sequence. The imaging parameters are listed in Table 1. The first two datasets were acquired with an 8-channel head coil and a Plexiglas phantom designed to measure image distortions filled with a 1:100 Gd-DTPA:water solution. In the third dataset, a vessel phantom, was visualized using a 6-channel spine array coil. For each dataset 50 measurements were performed. The reference image S^G for the SNR evaluation (Eq. [12]) was obtained as an average over all 50 acquisitions.

In Vivo Images

Three sets of in vivo head and chest images of a 25-year-old healthy volunteer after informed consent were obtained. A clinical 1.5T MR system with 32 receiver channels (Magnetom Avanto, Siemens Medical Solutions) was used. The imaging parameters are listed in Table 1. One set of sagittal head images at the midline as well as two sets of coronal images of the torso were acquired. Here, the averaging of many acquisitions was not possible because of patient movement. Therefore, a single image without aliasing was used as a reference for the SNR evaluation. This makes the quantitative results less significant.

PROBER Parameters

The reconstruction quality of PROBER was tested with several parameter settings on all simulated images with noise variance $\sigma_l^2 = 10^{-3}$. First, SNR was evaluated for the number of B-splines $I \times J$ varying from 4×4 to 14×14 (the estimation grid size was set to 128). Then the ideal

Table 1
Imaging Sequence Parameters of the Phantom and In Vivo Image Acquisitions

Set	TE [ms]	TR [ms]	Flip angle [°]	Slice thickness [mm]	Field of view [mm^2]	Dimensions [pixel^2]	Number of coils
Phantom 1	3.53	100	60	5	380 × 380	256 × 256	8
Phantom 2	3.53	100	60	5	200 × 200	256 × 256	8
Phantom 3	3.86	8	25	5	400 × 400	256 × 256	6
In vivo 1	10	100	25	7.8	250 × 250	256 × 256	14
In vivo 2	2.52	40	20	8.0	400 × 400	256 × 256	17
In vivo 3	2.52	40	20	8.0	400 × 400	256 × 256	24

estimation grid size was sought by experimenting with sizes from 24 to 192 pixels (9 × 9 B-splines were used).

Two different parameter settings termed PROBER A and B were used for the comparison with GRAPPA and SENSE. They focused on the reconstruction speed (PROBER A) and quality (PROBER B). In PROBER A, 5 × 5 B-splines were used with an estimation grid size 76 pixels. In PROBER B, 9 × 9 B-splines were used with a grid size of 128 pixels; the unaliased images were reconstructed for each array-coil separately. The PROBER A and B methods were compared with the GRAPPA and SENSE methods on all simulated, phantom, and in vivo datasets as specified in the previous sections.

Reconstruction Speed

The speed of the PROBER reconstruction was compared with the speed of the commercial implementations of the GRAPPA and SENSE algorithms. The speed was tested on the simulated dataset 1 (8 receiver coils) and dataset 2 (5 receiver coils) with image sizes from 64 × 64 to 768 × 768 pixels and an acceleration factor of 2. All methods were implemented in C++ and the tests were performed on an AMD K8 4.4 GHz processor with 4GB RAM. The total time of the estimation and the reconstruction processes was measured 30 times and the minimal value was considered.

RESULTS

Figure 1 shows the reconstruction SNR as a function of the number of B-splines $I \times J$ used. The SNR for each dataset was normalized by scaling the maximal value to 1 and the mean value over all simulated datasets is shown. The mean normalized SNR of PROBER as a function of the estimation grid size is shown in Fig. 2d. Aliasing artifacts are clearly visible on images corresponding to grid sizes of less than 76 pixels. For grid sizes of more than 76 pixels, no significant artifacts are visible (Fig. 2b,c).

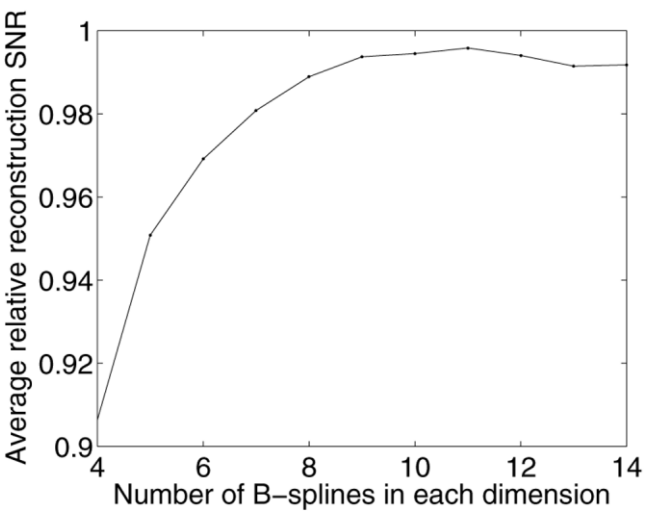

FIG. 1. Dependency of SNR on the number of B-splines used to represent the reconstruction transformation α in the estimation process. The normalized SNR averaged over all sets of simulated images with the noise variance 10^{-3} is shown.

The reconstruction SNR of PROBER, GRAPPA, and SENSE for simulated datasets is displayed in Fig. 3. PROBER B has the highest SNR for input images with SNR over 35 dB in 91% of the cases. For noisy images (under 35 dB), PROBER B has the highest SNR in 56% of cases. PROBER B has more than 2% higher SNR than PROBER A in all cases. Examples of reconstruction are shown in Fig. 4.

The reconstruction SNRs of the phantom and in vivo images are listed in Table 2. PROBER B and GRAPPA are free of visible aliasing artifacts on all tested phantom images, whereas there are minor aliasing artifacts in the PROBER A and SENSE reconstructions (Fig. 5). There are some artifacts in the GRAPPA, SENSE, and PROBER A reconstructions and only minor artifacts in the PROBER B reconstruction of the in vivo dataset 1 (Fig. 6). Reconstructed images of datasets 2 and 3 contain no visible aliasing artifacts except for SENSE and PROBER A reconstructions, which contain a few artifacts near the image edges.

Results for an acceleration factor of 4 on simulated datasets with noise variance $5 \cdot 10^{-4}$ are shown in Table 3. Most of the datasets are not suitable for reconstruction due to unfavorable coil configuration. Reconstructions of datasets 1, 3, and 5 all contain significant artifacts or are contaminated by noise; thus, a quantitative evaluation of SNR is not meaningful. GRAPPA has the highest SNR for datasets 2 and 4. For the rest of the datasets the PROBER SNR is 5–15% higher than SNR of the other methods. Examples of reconstruction are shown in Fig. 7.

Graphs in Fig. 3j,k show the reconstruction times for 5 and 8 receiver coils, respectively. The reconstruction times of PROBER A are the shortest for image sizes over 180 × 180 pixels (for five coils) and over 140 × 140 pixels (for eight coils). The PROBER B method has the longest reconstruction times for all tested image sizes.

DISCUSSION

PROBER Parameters

The accuracy of the reconstruction transformation approximation increases with a higher number of B-splines *I, J* and, thus, the reconstruction quality improves. However, for more than 9 × 9 B-splines the transformation becomes less constrained and more susceptible to noise. The quality also increases with higher estimation grid size because the error is evaluated more accurately. For the fast settings (PROBER A), the smallest reasonable parameter values were selected—5 × 5 B-splines with grid size 76 pixels. PROBER A offers reasonable suppression of aliasing artifacts as well as low amplification of noise. However, its reconstruction quality is lower than that of SENSE and GRAPPA. Thus, PROBER A should be used in applications where the reconstruction speed is the most important aspect. For the high-quality settings (PROBER B), the optimal values in terms of quality were selected—9 × 9 B-splines with the grid size 128 pixels (as the improvement in quality for more than 128 pixels and more than 9 × 9 B-splines is less than 1%). This is done at the cost of higher computational complexity. However, the difference with respect to SENSE and GRAPPA is at most 4 sec for the largest images tested.

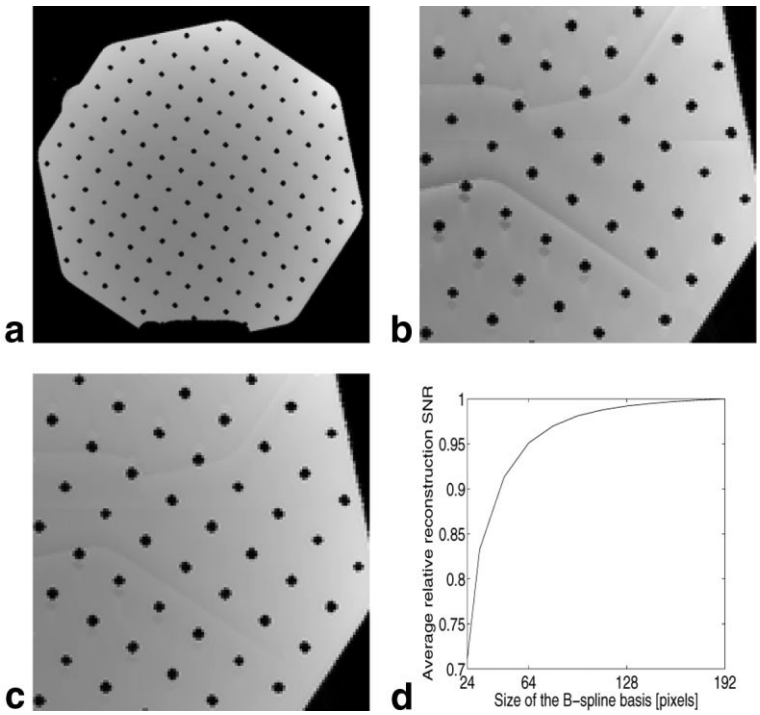

FIG. 2. A simulated image of a distortion phantom (**a**) undersampled with an acceleration factor of 2 is reconstructed using the PROBER method with a varying estimation grid size. Aliasing artifacts are visible for grid sizes of (**b**) 24 and (**c**) 48 pixels. The graph (**d**) shows the dependency of the mean normalized reconstruction SNR on the grid size.

The PROBER quality can be further improved by using a continuous representation of the B-splines (Eq. [8]) and of the reconstruction error (Eq. [9]). In order to do that, the reference images S_l have to be converted to a continuous representation using a continuous basis function Ψ. The main computational effort in this case lies in evaluating the scalar product of continuous functions Ψ and B-spline functions ψ. This can be estimated numerically and computed in advance to decrease the computational load of the reconstruction. Therefore, the quality can be improved without increasing the reconstruction speed [14]. This, however, is out of the scope of this article.

Comparison with SENSE

The idea of the Cartesian SENSE is to calculate the unfolded image as a weighted linear combination of the aliased images (Eq. [3]). The SENSE reconstruction weights are estimated for each location separately using smoothed sensitivity maps. The PROBER reconstruction equation (Eq. [3]) neglecting the B-spline approximation is similar to the SENSE equation (8). Unlike in SENSE (8), the PROBER reconstruction transformation is estimated at once by minimizing the assumed reconstruction error. In PROBER the reconstruction transformation is approximated using B-splines (Eq. [8]). This significantly reduces the number of unknown parameters and, thus, the reconstruction can be estimated for all pixels at once. This has a positive effect on the reconstruction speed. PROBER A is faster than SENSE for all image sizes captured with five receiver coils. For eight coils, PROBER A is faster for images larger than 128×128 pixels. The relative difference in speed is more significant for large images; PROBER A is 4 times faster than SENSE for eight coils and images of 768×768 pixels.

The B-spline approximation in PROBER has an implicit regularization effect and makes the estimation robust to noise in the reference images. Therefore, it is possible to calibrate PROBER using raw images without having to smooth the raw data. The PROBER B SNR on low-noise simulated images (SNR over 35 dB) is the same or higher than the SENSE SNR. This means that the artifact suppression of PROBER B is better. On the other hand, SENSE amplifies noise less than PROBER. This is evident from results on noisy images (SNR under 35 dB), where the PROBER SNR is comparable to or not more than 3% smaller than the SENSE SNR on all datasets. However, the results for noisy images are less important for clinical purposes.

In PROBER, the smooth reconstruction transformation is estimated by minimizing the total reconstruction error. Thus, the high-signal regions partly compensate for regions lacking the signal. This makes the estimation more reliable in areas where the signal voids. The effect of this can be seen in Figs. 4, 6, and 7, where the SENSE reconstructions contain many aliasing artifacts due to imperfect estimation of sensitivity in the low-signal areas, whereas the PROBER reconstructions are almost aliasing-free.

Phantom and in vivo results show an improved reconstruction quality of PROBER over SENSE. This is mainly due to a higher number of aliasing artifacts in the SENSE reconstruction (Figs. 5, 6). The factor 4 SENSE reconstructions contain in general low noise; however, due to the presence of aliasing artifacts the SENSE SNR is lower than the PROBER B SNR on all simulated datasets.

Comparison with GRAPPA

The GRAPPA method operates in *k*-space to reconstruct the missing *k*-space lines as a linear combination of several

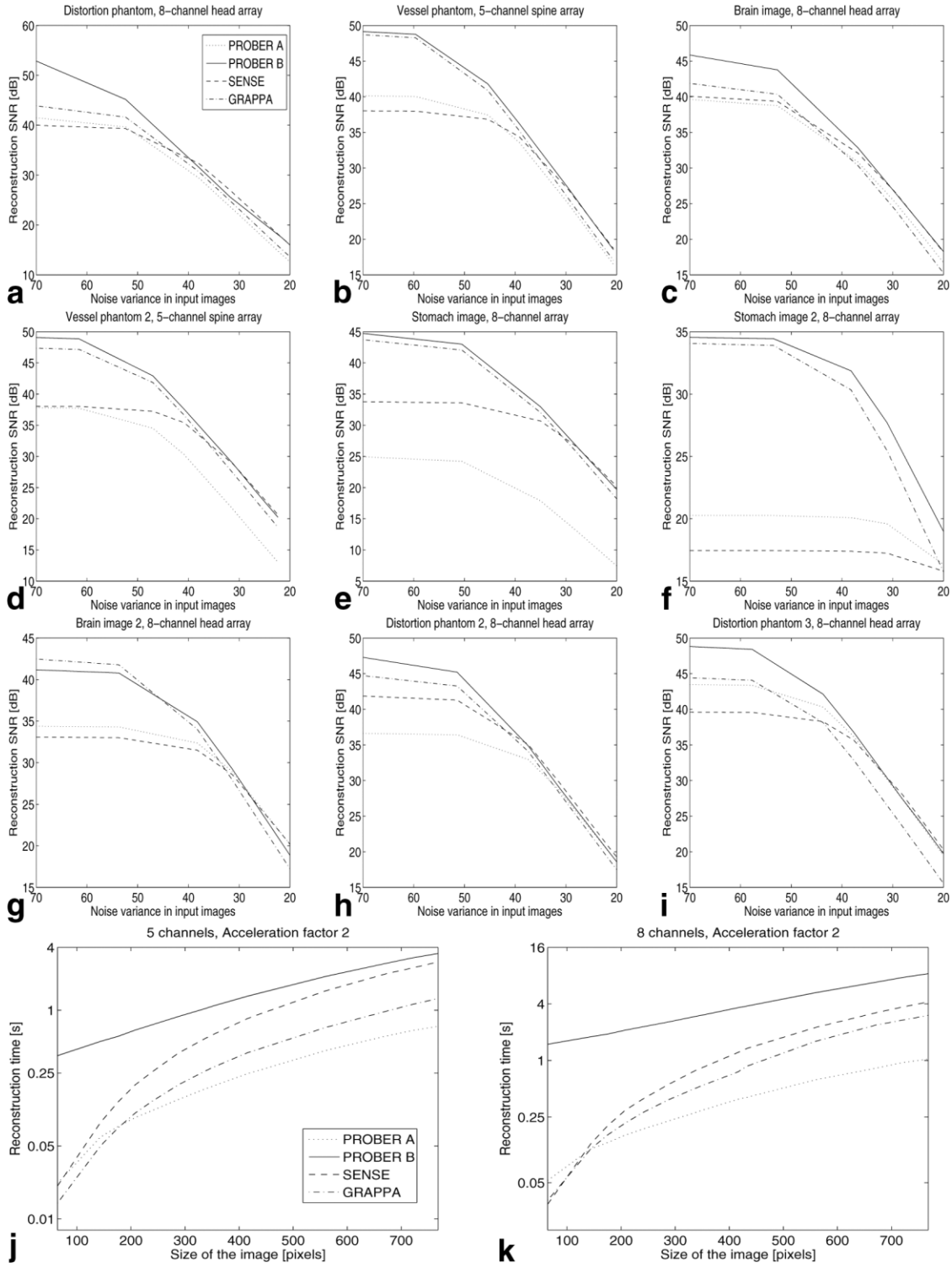

FIG. 3. SNR of SENSE, GRAPPA, and PROBER on nine simulated datasets with an acceleration factor of 2 and input image SNR from 70 dB down to 20 dB (**a–i**). Reconstruction times for (**j**) five and (**k**) eight receiver channels and image of 64 × 64 to 768 × 768 pixels.

adjacent lines (Eq. [13]) (7). PROBER can be viewed as an image-domain version of GRAPPA that differs in the choice of the basis functions (see Appendix). In GRAPPA, harmonic functions are used to represent the reconstruction weights (Eq. [15]), while B-splines are used in PROBER (Eq. [16]). B-splines are spatially localized and they have good properties for the approximation of smooth continuous functions [15] such as sensitivity maps and their inverse. The harmonic functions are localized in frequency, which is advantageous for the *k*-space reconstruction but it can be less effective for certain coil configurations (14).

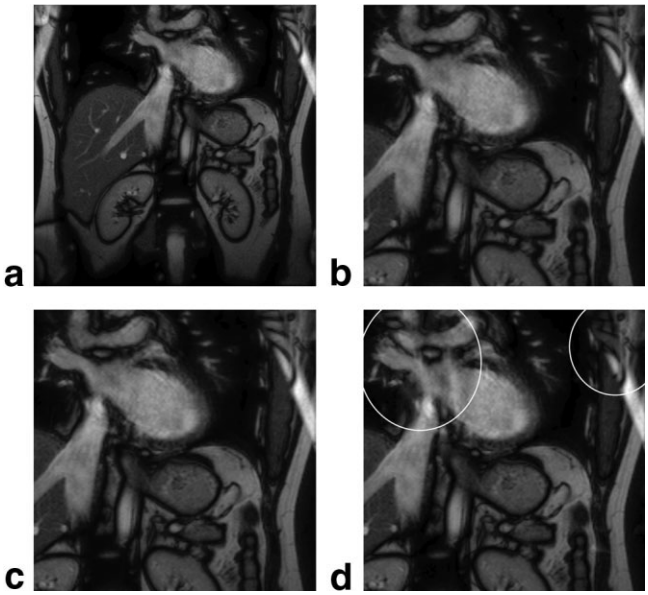

FIG. 4. Reconstructions of the simulated dataset 6 undersampled with a factor 2 (see also Fig. 3f). (**a**) Original image, (**b**) GRAPPA (34.1 dB), (**c**) PROBER B (34.5 dB), (**d**) SENSE (17 dB). The reconstructed images (**b–d**) are cropped. The PROBER and GRAPPA reconstructions have high SNR and are free of aliasing artifacts. (**d**) The SENSE method failed in this image, producing noticeable divergence from the original image—as marked by white circles.

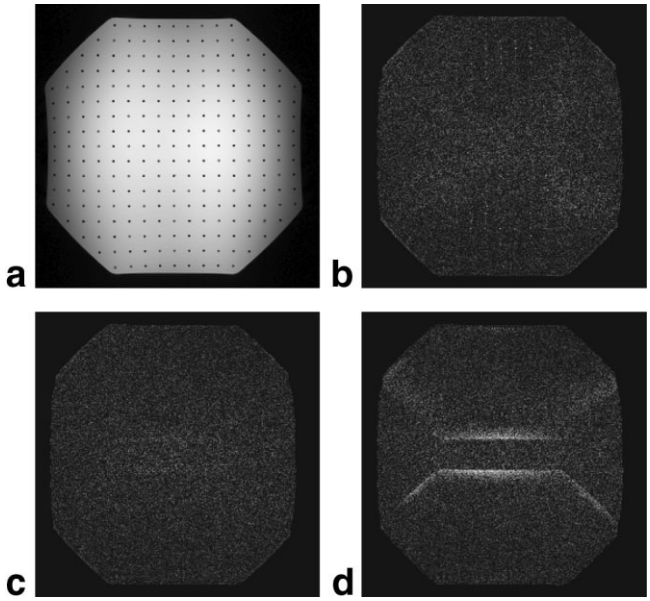

FIG. 5. Reconstructions of the phantom dataset 1 with an acceleration factor of 2. The difference between the original image (**a**) and the reconstructed images is shown to facilitate comparison. (**a**) Original image; difference images for (**b**) GRAPPA (37.0 dB), (**c**) PROBER B (37.6 dB) and (**d**) SENSE (35.8). GRAPPA and PROBER reconstructions (**b**) and (**c**) are free of significant aliasing artifacts. There are visible fold-over artifacts in the SENSE reconstruction (**d**).

The PROBER B method achieves a higher SNR than GRAPPA on most of the simulated datasets for all input noise variances (Fig. 3). The advantage of PROBER B is visible especially on datasets 1, 3, and 9 (Fig. 3a,c,i) that have an unfavorable coil configuration for GRAPPA, as the harmonics functions are not optimal. However, the PROBER B method using B-spline approximation reaches good results on these datasets.

Another advantage of B-splines is their better approximation properties, i.e., a lower number of basis functions can be used to approximate the reconstruction transformation with the same precision. Even 5×5 B-splines used in PROBER A are sufficient, which makes PROBER A faster than GRAPPA for images larger than 180×180 (for five coils) and 140×140 pixels (for eight coils). For eight coils and image size 768×768 pixels, PROBER A is 3 times faster than GRAPPA.

As stated in the Results section, PROBER B reaches better quality than GRAPPA on most of the datasets. PROBER B has a 1–15% better SNR than GRAPPA on more than half of the simulated datasets for all tested noise levels. It has also a 1–7% higher SNR on all phantom images. For in vivo dataset 1, PROBER achieves 5% higher SNR than GRAPPA and the PROBER SNR for datasets 2 and 3 is comparable to the GRAPPA SNR. For acceleration

Table 2
Reconstruction SNR of the Phantom and In Vivo Datasets (in dB)

Set	PROBER A	PROBER B	SENSE	GRAPPA
Phantom 1	27.2	37.6	35.8	37.0
Phantom 2	32.3	35.9	34.3	33.5
Phantom 3	25.3	26.3	26.1	26.1
In vivo 1	20.1	27.2	22.4	26.0
In vivo 2	17.2	26.8	18.7	26.8
In vivo 3	15.0	22.9	16.1	23.1

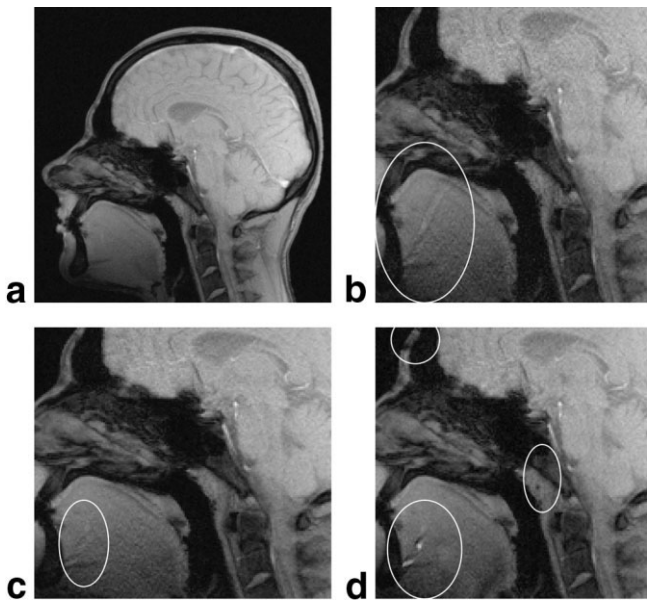

FIG. 6. Reconstructions of the in vivo dataset 1 with an acceleration factor of 2. (**a**) Original image, (**b**) GRAPPA (26.0 dB)—small number of artifacts, higher level of noise, (**c**) PROBER B (27.2 dB)—minor artifacts, (**d**) SENSE (22.4 dB)—high number of visible artifacts. Detailed images of the reconstructions are shown. White ellipses mark aliasing artifacts.

Table 3
Reconstruction SNR of Simulated Datasets for an Acceleration Factor of 4 (in dB)

Method \ Set	1	2	3	4	5	6	7	8	9
PROBER A	13.1	21.6	11.3	22.3	15.2	14.3	16.5	12.1	20.9
PROBER B	17.9	28.3	17.9	27.6	21.6	19.5	24.5	24.7	28.0
SENSE	13.3	18.5	12.6	22.6	13.0	9.0	16.7	22.4	24.0
GRAPPA	18.3	28.5	18.4	27.7	22.1	17.5	22.6	23.5	21.7

factor of 4, GRAPPA shows fewer artifacts than PROBER for datasets 2 and 4. This is because the spine array-coil sensitivities change mainly in the phase-encoding direction and are favorable for GRAPPA. For the rest of the datasets PROBER has higher SNR than GRAPPA. Specifically, PROBER reached a significantly higher SNR than GRAPPA with a lower level of aliasing on dataset 6 (Fig. 7). The results on the factor 4 reconstructions show that PROBER reconstruction can be used where other reconstruction techniques fail.

CONCLUSION

A new reconstruction method, PROBER, was proposed and implemented. The speed and quality of the method was compared with the commercial methods GRAPPA and SENSE. It was shown that it is possible to achieve higher reconstruction quality with PROBER than with SENSE and GRAPPA for certain input images. It was also shown that PROBER is faster than the other two methods for image resolutions of more than 150 × 150 pixels at the cost of slightly lower reconstruction quality. Therefore, the PROBER method offers a good alternative to present reconstruction methods. Options to improve the algorithm were indicated. This should lead to the same reconstruction quality as GRAPPA and SENSE at higher reconstruction speed.

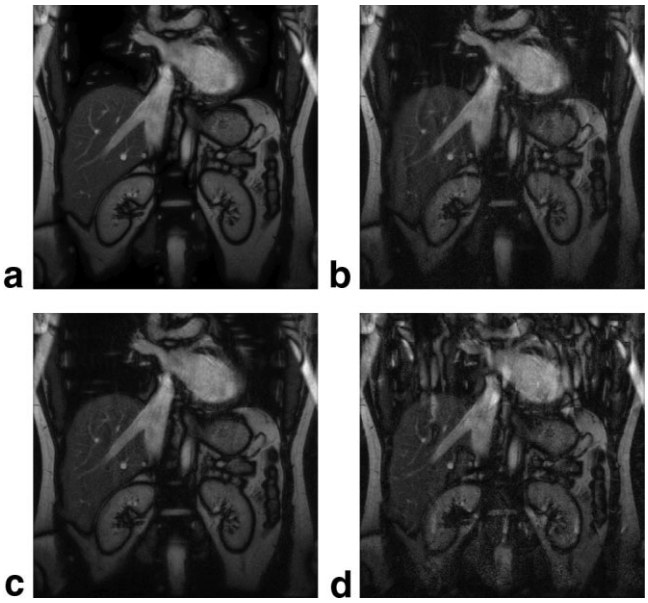

FIG. 7. Reconstructions of the simulated dataset 6 with an acceleration factor of 4 (see Figs. 3d, 4 for the results with an acceleration factor of 2). Images were undersampled along the horizontal axis. (**a**) Original image, (**b**) GRAPPA (17.5 dB)—minor artifacts, (**c**) PROBER B (19.5 dB), (**d**) SENSE (9.0 dB)—major artifacts over the whole image.

APPENDIX

The main difference between the PROBER and GRAPPA reconstruction methods is that the first operates in the image domain and the second in *k*-space. Here, it is shown that these methods are theoretically similar and differ only in the choice of the basis functions. GRAPPA reconstructs the missing *k*-space lines using the reconstruction coefficients w (7):

$$\hat{s}_j(k-m) = \sum_{l=1}^{L} \sum_{b=0}^{N_b-1} w(j,b,l,m) s_l(k-bM), \quad [13]$$

where N_b is the number of blocks used in the reconstruction, M is the acceleration factor, k goes through the acquired lines ($k=0, M, 2M,\ldots, N_y\text{-}1$) and m goes from 1 to $M\text{-}1$. The acquired lines need not be reconstructed ($\hat{s}_j(k) = s_l(k)$), thus, the weights n can be defined also for $m=0$ as $w(j,0,j,0)=1$ and $w=0$ elsewhere. Then Eq. [13] can be rewritten for $ky = 0, 1, \ldots, N_y\text{-}1$. Without loss of generality the weights $w(j,b,l,m)$ can be replaced by $w(j,bM,l,m)$ and the indices bM and m can then be grouped together:

$$\hat{s}_j(k_y) = \sum_{l=1}^{L} \sum_{k'_y=k_y-bM}^{k_y+M-1} w(j, k_y \mod M + k_y - k'_y, l, k_y \mod M) s_l(k'_y) \delta_{0,k'_y \mod M}$$

$$\hat{s}_j(k_y) = \sum_{l=1}^{L} \sum_{k'_y=k_y-bM}^{k_y+M-1} w(j, k_y - k'_y, l) s_l(k'_y) \delta_{0,k'_y \mod M} \quad [14]$$

where δ is the Kronecker delta. The images s in Eq. [14] are transformed to the images S and the parameters w are Fourier transformed to W. After several rearrangements, the weights W are transformed back to the Fourier domain and then Fourier transformation is applied to the whole equation:

$$\sum_{y=0}^{N_y-1} e^{i2\pi y k_y} \hat{S}_j(y) = \sum_{l=1}^{L} \sum_{k'_y=k_y-bM}^{k_y+M-1} \sum_{y=0}^{N_y-1} e^{i2\pi y k'_y} S_l^A(y) \frac{1}{N_y} \sum_{y'=0}^{N_y-1} e^{i2\pi y'(k_y-k'_y)} W_{jj}(y')$$

$$\sum_{y=0}^{N_y-1} e^{i2\pi y k_y} \hat{S}_j(y)$$

$$= \sum_{l=1}^{L} \sum_{y=0}^{N_y-1} e^{i2\pi y k_y} S_l^A(y) \sum_{k'_y=-bM}^{M-1} e^{i2\pi y k'_y} \frac{1}{N_y} \sum_{y'=0}^{N_y-1} e^{-i2\pi y' k'_y} W_{j,l}(y')$$

$$\sum_{y=0}^{N_y-1} e^{i2\pi y k_y} \hat{S}_j(y) = \sum_{l=1}^{L} \sum_{y=0}^{N_y-1} S_l^A(y) \sum_{k'_y=-bM}^{M-1} e^{i2\pi y k'_y} w_{j,l}(k'_y) e^{i2\pi y k_y}$$

$$\hat{S}_j(y) = \sum_{l=1}^{L} S_l^A(y) \sum_{k'_y=-bM}^{M-1} e^{i2\pi y k'_y} w_{j,l}(k'_y) \qquad [15]$$

The GRAPPA reconstruction equation after the Fourier transformation (Eq. [15]) is similar to the PROBER reconstruction (Eqs. [3,8]):

$$\hat{S}_j(y) = \sum_{l=1}^{L} S_l^A(y) \sum_{i=1}^{I} g_{iji} \varphi_i(y). \qquad [16]$$

Thus, GRAPPA (Eq. [15]) and PROBER (Eq. [16]) differ only in the choice of the basis function, where GRAPPA uses harmonic functions and PROBER uses B-splines.

REFERENCES

1. Sodickson DK, Manning W. Simultaneous acquisition of spatial harmonics (SMASH): fast imaging with radiofrequency coil arrays. Magn Reson Med 1997;38:591–603.
2. McKenzie CA, Yeh EN, Sodickson DK. Improved spatial harmonic selection for SMASH image reconstructions. Magn Reson Med 2001; 46:831–836.
3. Sodickson DK. Tailored SMASH image reconstruction for robust in vivo parallel MR imaging. Magn Reson Med 2000;44:243–251.
4. Jakob PM, Griswold MA, Edelman RR, Sodickson DK. AUTO-SMASH: a self-calibrating technique for SMASH imaging. In: Proceedings of the 6th Annual Meeting of ISMRM, Sydney, 1998. p 1975.
5. Griswold MA, Jakob PM, Nittka M, Goldfarb JW, Haase A. VD-AUTO-SMASH imaging. Magn Reson Med 2001;45:1066–1074.
6. Bydder M, Larkman DJ, Hajnal JV. Generalized SMASH imaging. Magn Reson Med 2002;47:160–170.
7. Griswold MA, Jakob PM, Heidemann RM, Nittka M, Jellus V, Wang J, Kiefer B, Haase A. Generalized autocalibrating partially parallel acquisitions (GRAPPA). Magn Reson Med 2002;47:1202–1210.
8. Pruessmann KP, Weiger M, Sheidegger MB, Boesiger Peter. SENSE: sensitivity encoding for fast MRI. Magn Reson Med 1999;42:952–962.
9. Pruessmann KP, Weiger M, Börnert P, Boesiger P. Advances in sensitivity encoding with arbitrary k-space trajectories. Magn Reson Med 2001;46:638–651.
10. Sodickson DK, McKenzie CA. A generalized approach to parallel magnetic resonance imaging. Med Phys 2001;28:1629–1643.
11. Larsson EG, Erdogmus D, Yan R, Principe JC, Fitzsimmons JR. SNR-optimality of sum-of-squares reconstruction for phased-array magnetic resonance imaging. J Magn Reson 2003;163:121–123.
12. Petr J, Kybic J, Müller S, Bock M, Hlaváč V. Parallel MRI reconstruction using B-spline approximation. In: Proceedings of the 13th Scientific Meeting and Exhibition of ISMRM, Miami, FL, 2005. p 2421.
13. Petr J, Kybic J, Hlaváč V, Müller S, Bock M. Fast parallel MRI reconstruction using B-spline approximation (PROBER). In: Proceedings of SPIE Medical Imaging 2006: Physics of Medical Imaging, San Diego, 2006. p 1251–1262.
14. Petr J. Parallel magnetic resonance imaging reconstruction. PhD thesis. Czech Technical University, Prague, 2007.
15. Unser M. Splines: a perfect fit for signal and image processing. IEEE Signal Proc 1999:22–38.
16. Golub GH, Van Loan CF. Special Linear Systems. In: Matrix computations, 2nd ed. Baltimore: John Hopkins University Press; 1989.
17. Press WH, Teukolsky SA, William T, Flannery BP. Solution of Linear Algebraic Equations. In: Numerical recipes in C++: the art of scientific computing, 2nd ed. Cambridge, UK: Cambridge University Press; 2002.
18. McKenzie CA, Yeh EN, Ohliger MA, Price MD, Sodickson DK. Self-calibrating parallel imaging with automatic coil sensitivity extraction. Magn Reson Med 2002:47:529–538.
19. Sled JG, Zijdenbos AP, Evans AC. A nonparametric method for automatic correction of intensity non-uniformity in MRI data. IEEE Trans Med Imaging 1998;17:87–97.